



Stretchable colour-sensitive quantum dot nanocomposites for shape-tunable multiplexed phototransistor arrays

Jun-Kyul Song^{1,2,3,12}, Junhee Kim^{1,2,3,12}, Jiyong Yoon^{1,2,3,12}, Ja Hoon Koo^{1,3,12}, Hyunjin Jung^{4,5}, Kyumin Kang^{1,2,3}, Sung-Hyuk Sunwoo^{1,2,3}, Seungwon Yoo^{1,6}, Hogeun Chang^{1,2,3}, Jinwoung Jo^{1,2,3}, Woonhyuk Baek^{1,2,3}, Sanghwa Lee^{1,2,3}, Mincheol Lee^{1,3}, Hye Jin Kim^{1,3}, Mikyung Shin^{4,7}, Young Jin Yoo^{1,2,3}, Young Min Song^{1,2,3}, Taeghwan Hyeon^{1,2,3,6}✉, Dae-Hyeong Kim^{1,2,3,6,9}✉ and Donghee Son^{1,4,5,10,11}✉

High-performance photodetecting materials with intrinsic stretchability and colour sensitivity are key requirements for the development of shape-tunable phototransistor arrays. Another challenge is the proper compensation of optical aberrations and noises generated by mechanical deformation and fatigue accumulation in a shape-tunable phototransistor array. Here we report rational material design and device fabrication strategies for an intrinsically stretchable, multispectral and multiplexed $5 \times 5 \times 3$ phototransistor array. Specifically, a unique spatial distribution of size-tuned quantum dots, blended in a semiconducting polymer within an elastomeric matrix, was formed owing to surface energy mismatch, leading to highly efficient charge transfer. Such intrinsically stretchable quantum-dot-based semiconducting nanocomposites enable the shape-tunable and colour-sensitive capabilities of the phototransistor array. We use a deep neural network algorithm for compensating optical aberrations and noises, which aids the precise detection of specific colour patterns (for example, red, green and blue patterns) both under its flat state and hemispherically curved state (radius of curvature of 18.4 mm).

Shape-tunable photodetector arrays, integrated with appropriate optical systems, have distinctive advantages, such as a wide field of view, low optical aberration and tunable focal length^{1–4}. A unique feature of such photodetector arrays, namely, its active adaptation to time-dynamic surfaces with three-dimensional hierarchical geometry^{5,6}, makes them a key element for electronic eyes and artificial vision systems. Various efforts have been made to improve the optoelectronic performance and mechanical stability of shape-tunable imaging systems. One approach is to adopt ultrathin inorganic photosensitive semiconducting materials together with strain-dissipative device designs, such as non-planar pop-up structures^{7,8}, serpentine-shape interconnects^{9–11} and kirigami-based designs^{12–14}. These device structures allow non-stretchable photosensitive materials to maintain their electrical performance under mechanical deformations. However, such a structural design approach for shape tunability requires complex fabrication processes^{15–17}, and even more complicated material considerations and process conditions are necessary for colour selectivity. Further, an undesirable issue associated with the limited areal density, due to the use of strain-dissipative interconnects, still remains.

Another approach to develop a shape-tunable photodetector array is to adopt intrinsically stretchable materials^{18–22}, which does not require the use of special device designs and geometries. Elastic

conductors and semiconductors using a mixture of organic/polymeric materials and elastomers have been employed to develop intrinsically stretchable transistor arrays, sensor arrays and circuits^{23–26}. However, there are still challenges in terms of the performance and durability of materials and devices, particularly under severe repetitive mechanical deformations, as well as multispectral sensing and wide field-of-view imaging capability (Supplementary Table 1)^{27–32}. In this regard, a stretchable photosensitive semiconducting material that leverages both high-performance inorganic photosensitive materials^{27–29} and soft polymeric charge transport materials^{30–32} can be promising for intrinsically stretchable photodetectors. Furthermore, additional measures that can compensate for optical aberrations and noises occurring from dynamic device deformations and related mechanical fatigue accumulations, which consequently result in electrical/optical performance degradation, are highly required for shape-tunable imaging systems.

Here we report a rational material design and facile device fabrication strategy for an intrinsically stretchable, multispectral and multiplexed phototransistor array. The colour-sensitive, shape-tunable characteristics of the phototransistor array are achieved using an intrinsically stretchable quantum dot (QD)-based semiconducting nanocomposite (isQDSN) composed of an organic semiconducting polymer, size-tunable QDs and an elastomeric matrix. Specifically,

¹Center for Nanoparticle Research, Institute for Basic Science (IBS), Seoul, Republic of Korea. ²School of Chemical and Biological Engineering, Seoul National University, Seoul, Republic of Korea. ³Institute of Chemical Processes, Seoul National University, Seoul, Republic of Korea. ⁴Department of Electrical and Computer Engineering, Sungkyunkwan University, Suwon, Republic of Korea. ⁵Center for Neuroscience Imaging Research, Institute for Basic Science (IBS), Suwon, Republic of Korea. ⁶Interdisciplinary Program for Bioengineering, Seoul National University, Seoul, Republic of Korea. ⁷Department of Intelligent Precision Healthcare Medicine, SKKU Institute for Convergence, Sungkyunkwan University, Suwon, Republic of Korea. ⁸School of Electrical Engineering and Computer Science, Gwangju Institute of Science and Technology, Gwangju, Republic of Korea. ⁹Department of Materials Science and Engineering, Seoul National University, Seoul, Republic of Korea. ¹⁰Department of Superintelligence Engineering, Sungkyunkwan University, Suwon, Republic of Korea. ¹¹KIST-SKKU Carbon-Neutral Research Center, Sungkyunkwan University (SKKU), Suwon, Republic of Korea. ¹²These authors contributed equally: Jun-Kyul Song, Junhee Kim, Jiyong Yoon, Ja Hoon Koo. ✉e-mail: thyeon@snu.ac.kr; dkim98@snu.ac.kr; daniel3600@g.skku.edu

a unique spatial distribution of QDs is formed within the isQDSN due to surface energy mismatch, achieving high photosensitivity. Furthermore, critical challenges associated with optical aberrations and noises of the shape-tuned multiplexed phototransistor array were resolved by adopting a deep neural network (DNN) algorithm. The multiplexed phototransistor array enabled the precise detection of red/green/blue colour patterns in its flat as well as deformed states.

Shape-tunable multiplexed isQDSN-based phototransistor array

The isQDSN was fabricated by combining inorganic semiconducting nanocrystals, a fibril-type semiconducting polymer and an elastomer (Fig. 1a). Specifically, size-tunable CdSe/ZnS core/shell-type QDs were used for multispectral photoabsorption, semiconducting polymer fibril (poly[2,5-(2-octyldodecyl)-3,6-diketopyrrolopyrrole-*alt*-5,5-(2,5-di(thien-2-yl)thieno [3,2-*b*]thiophene)] (PDPP2T-TT-OD)) was used for facile charge transport through their percolated network with QDs and polystyrene-*block*-poly(ethylene-*ran*-butylene)-*block*-polystyrene (SEBS) was used as an elastomer matrix.

The isQDSN was employed as a channel material to fabricate a multiplexed array of intrinsically stretchable phototransistors ($5 \times 5 \times 3$; Fig. 1b, left). For stretchable dielectric and electrodes, spin-coated SEBS and microcracked gold (Au) nanomembranes were used, respectively. The $5 \times 5 \times 3$ array was fabricated by stacking three layers of 5×5 phototransistor arrays for detecting multispectral optical inputs (for example, blue (B), green (G) and red (R) light; Fig. 1b, right (top to bottom)). Each RGB pixel was integrated in a misaligned manner. The multiplexed array is intrinsically stretchable (Fig. 1c, right), and consequently, special structural designs are not needed to accomplish shape tunability. Moreover, we applied a deep learning algorithm^{33,34} to compensate for optical aberrations and noise during mechanical deformations of the phototransistor arrays (Fig. 1d), enhancing photodetection accuracy.

Material characterization of the isQDSN film

The isQDSN was fabricated by mixing QDs (R, G or B QDs), PDPP2T-TT-OD and SEBS with an optimized weight fraction (Fig. 2a and Methods). The optimal mixing ratio that results in both high optoelectronic performance and stretchability has been systematically investigated, by correlating the structural analysis results of isQDSNs with various mixing ratios (Extended Data Fig. 1 and Supplementary Note 1) and the results of phototransistor performance analysis employing the corresponding isQDSNs (Extended Data Figs. 2 and 3 and Supplementary Note 2). The atomic ratios of each component and isQDSN were characterized using an elemental analysis and inductively coupled plasma analysis (Supplementary Tables 2 and 3). The fabricated isQDSN films were characterized using cross-sectional high-resolution transmission electron microscopy (HRTEM) (Fig. 2b). Another cross-sectional HRTEM image for the magnified views of the top (red dotted) and bottom (blue dotted) of the film (Supplementary Fig. 1) showed that the QDs are mostly observed at the top and bottom surfaces of the film. The isQDSN exhibited a smooth surface with a root mean square roughness (R_{rms}) of ~ 3.998 nm (Supplementary Fig. 2, atomic force microscopy image). The line-scan data of the energy-dispersive X-ray spectrum in the depth direction and depth-profiling X-ray photoelectron spectrometer (depth XPS) data of elemental zinc confirm the high concentration of zinc at the top and bottom of the film, which originates from the ZnS shell of CdSe/ZnS core/shell QDs³⁵ (Fig. 2c,d). In contrast, the electron energy loss spectroscopy data and depth XPS data of elemental carbon show that elemental carbon, which is mostly found in the SEBS elastomer, is at the centre of the film (Supplementary Fig. 3a,b).

Subsequently, we analysed the radiative decay dynamics of the carriers in the nanocomposite by measuring the time-resolved photoluminescence (PL) spectra. The PL decay lifetime of the isQDSN is shorter than that of pure green QDs (Fig. 2e), which implies that charge transfer occurs from the QDs to the semiconducting polymer in the nanocomposite due to the formation of electrically percolated pathways inside the blended film³⁶. Furthermore, transient absorption (TA) spectroscopy was employed to investigate the detailed carrier relaxation dynamics of our isQDSN by measuring differential transmitted power (T) of the probe with and without the excite pump, $\Delta T/T$. Ground-state bleaching (GSB), which is the depletion of electron population at the ground states, occurred at 600 nm probe wavelength (Fig. 2f, red dotted line) in QDs, whereas in the conducting polymer (PDPP2T) and in our isQDSN, GSB appeared at 850 nm (Fig. 2f, black and red solid lines, respectively). Furthermore, the increase in the GSB spectra in the isQDSN compared with that of the conducting polymer (Fig. 2g) demonstrates that the amount of excited carriers increased when QDs were blended with the conducting polymer. These results suggest that once the hot carriers are formed in the QDs, they instantly move to the conducting polymer (within 1 ps)³⁷. The charge transfer mechanism can also be explained by using the energy-band diagram (Fig. 2h) as well as the carrier mobility and activation energy analysis of the isQDSN-based phototransistors (Supplementary Note 3). Because the highest-occupied molecular orbital of PDPP2T is higher than the conduction-band energy level of QDs, holes generated in the QDs by external illumination can easily diffuse from the QDs to PDPP2T (ref. 38).

Intrinsically stretchable phototransistor characterization

Based on the isQDSN film, an intrinsically stretchable multiplexed phototransistor array was fabricated. For stretchable electrodes, an Au nanomembrane with a thickness of 50 nm was deposited on the SEBS substrate (thickness, ~ 200 μm). Supplementary Fig. 5 shows the stretching characteristics of the electrode³⁹. SEBS was also used as a gate dielectric (~ 1 μm) and encapsulation layer (~ 200 μm). The isQDSN films were used as the channel materials of bottom-gated phototransistors. QDs with various bandgaps (Supplementary Fig. 6 and Supplementary Note 4) were used to prepare three types of isQDSN film (RGB). Unless stated otherwise, the fabricated phototransistors have a channel length (L_{ch}) and width (W_{ch}) of 150 μm and 1.5 mm, respectively. Separately fabricated R, G and B phototransistor arrays were stacked into a multiplexed phototransistor array ($5 \times 5 \times 3$ array; 5×5 R-sensitive array at the bottom, 5×5 G-sensitive array in the middle and 5×5 B-sensitive array at the top) using a transfer technique. A schematic of the vertical structure and a photograph of the intrinsically stretchable phototransistor array are shown in Fig. 3a and its inset, respectively. The detailed fabrication process is shown in Supplementary Fig. 7.

The colour selectivity of the stretchable phototransistors was characterized. All the phototransistors in the $5 \times 5 \times 3$ phototransistor array exhibited low dark currents of ~ 20 pA. When blue light (450 nm) was applied to the phototransistor employing the blue-light-sensitive isQDSN (hereinafter referred to as a blue phototransistor and similarly for red and green phototransistors), the photocurrent increased to ~ 0.6 μA . The photocurrents of the blue phototransistor remained low (~ 10.0 nA and ~ 0.1 nA) on illumination with green light (525 nm) and red light (635 nm), respectively, showing colour selectivity (Fig. 3b). In the case of the green phototransistor, the photocurrent increased to ~ 0.2 μA when blue light and green light were illuminated and exhibiting a low photocurrent of ~ 10 nA for red light (Fig. 3c). The red phototransistor responded to all lights (R, G and B) and its photocurrent increased to ~ 0.2 μA (Fig. 3d).

The mechanical robustness of the intrinsically stretchable photodetectors was evaluated using a uniaxial stretching test

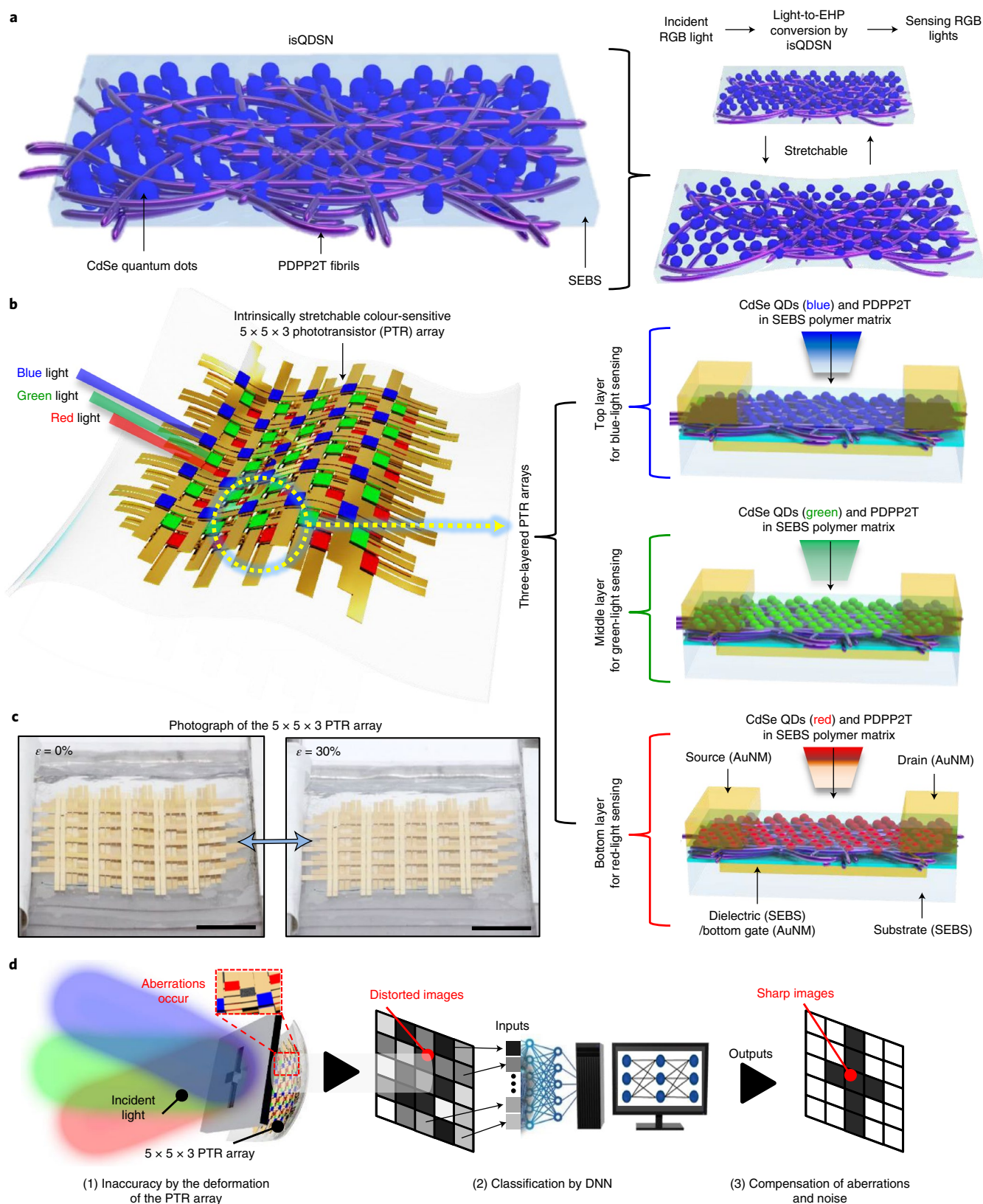


Fig. 1 | The isQDSN for the intrinsically stretchable phototransistor array. **a**, Schematic of the isQDSN, which consists of QDs and semiconducting polymer fibrils (PDPP2T) in the SEBS elastomer matrix. The isQDSN is capable of effectively converting electron-hole pairs (EHP) generated by an incident light into an electrical signal during pristine and stretched modes (right). **b**, Schematic showing the intrinsically stretchable phototransistor array using isQDSN as a photoabsorption layer. Different bandgaps of QDs enable colour selectivity (blue, green and red). **c**, Photographs of the integrated $5 \times 5 \times 3$ phototransistor array before stretching (left) and after 30% stretching (right). Scale bars, 10 mm. **d**, Schematic describing the procedure to enhance the accuracy of the phototransistor during mechanical deformations, using the deep learning algorithm.

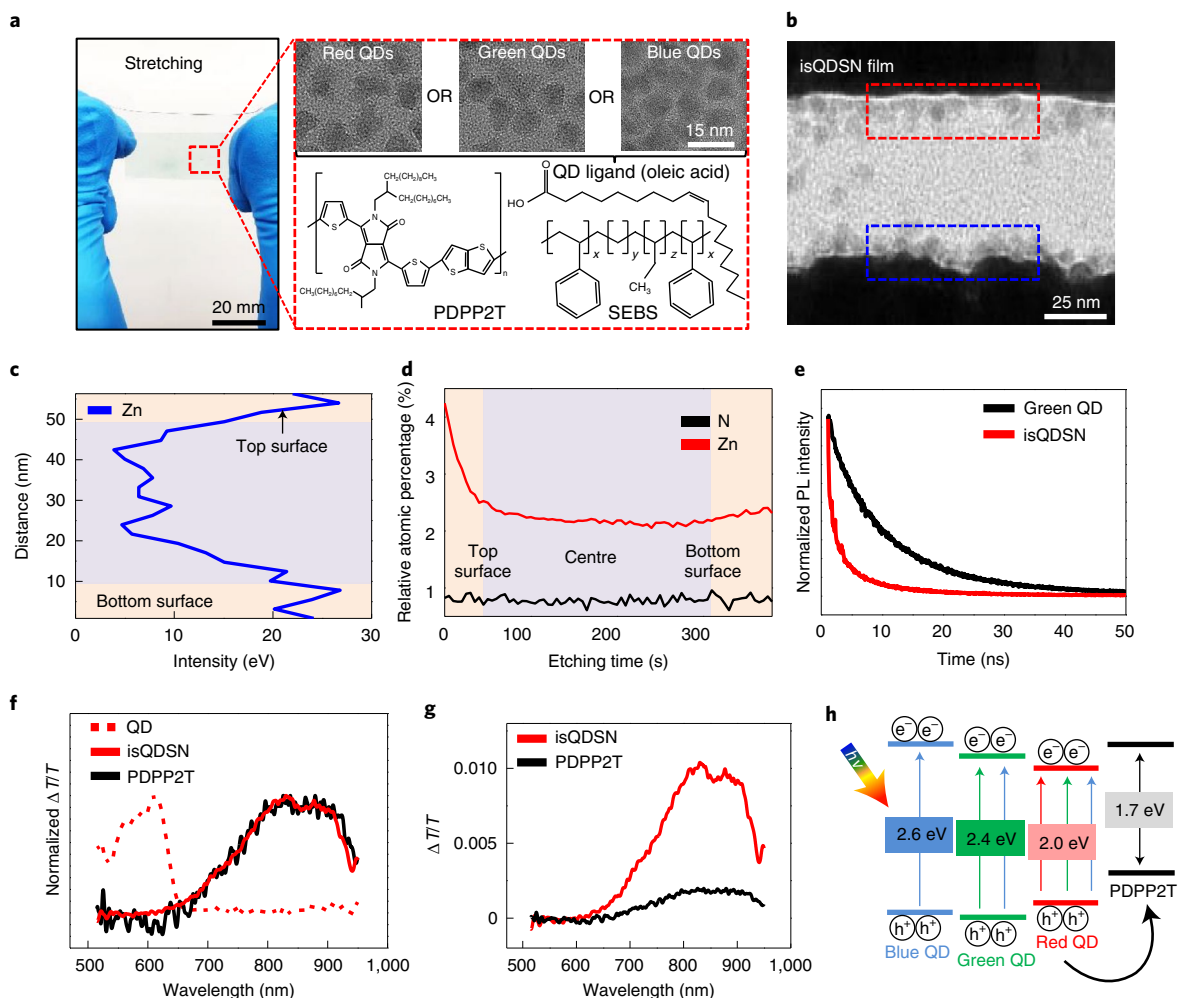


Fig. 2 | Material characterization of the isQDSN film. **a**, Photograph of the stretched isQDSN film attached on an SEBS handling substrate (50% stretching, left). Scale bar, 20 mm. The frames on the top right-hand side show the components of the isQDSN such as the transmission electron microscopy image of red, green and blue QDs with an oleic acid ligand (top) and molecular structure of PDPP2T and SEBS (bottom). Scale bar, 15 nm. **b**, Cross-sectional HRTEM image of the isQDSN film. Scale bar, 25 nm. **c**, Linescan energy-dispersive X-ray spectral result of zinc from the ZnS shell of the QDs in the isQDSN. **d**, Depth XPS spectra of nitrogen (black) and zinc (red) of the isQDSN film. **e**, Time-resolved PL spectra of green QDs and the isQDSN. **f**, Normalized TA spectra of the QD, PDPP2T and isQDSN films at 0.5 ps. **g**, TA spectra of the isQDSN and PDPP2T films at 0.5 ps. $\Delta T/T$, differential transmitted power of the probe with and without the excite pump. **h**, Schematic of the energy-band diagrams and hole movement by external illumination ($h\nu$). T, transmitted power.

(Supplementary Fig. 11). Even under an applied strain of 30%, along the direction perpendicular to the channel, the photoresponses of the R, G and B phototransistors to periodic on/off illumination showed minimal changes compared with those of unstretched phototransistors (Fig. 3e). The mechanical stability of the intrinsically stretchable photodetectors was further validated by analysing the change in photocurrents during 1,000 cyclic stretching tests at 30% strain and by analysing the cross-sectional structures using scanning electron microscopy after the cyclic stretching (Extended Data Fig. 4). Neither notable degradation in the optoelectronic performance nor any delamination and/or mechanical fractures were observed. The photoresponse times (τ_{rise} , τ_{fall}) and gate bias (V_G) of the blue phototransistor were $\tau_{\text{rise}} = 0.31$ s, $\tau_{\text{fall}} = 0.27$ s and $V_G = -15$ V. The intrinsically stretchable R, G and B phototransistors also exhibited stable normalized on currents with minimal variations (<5%) when stretched by 30% (Fig. 3f). Under a 30% strain, a photoresponsivity of ~ 0.013 mA W^{-1} and photodetectivity of $\sim 3.8 \times 10^6$ Jones were obtained from the green phototransistor illuminated with green light (Fig. 3g). The photoresponsivities and

photodetectivities of the blue and red phototransistors illuminated by blue and red light showed similar characteristic photoresponses (Supplementary Fig. 12). It should be noted that the phototransistors were still operable at an applied strain of 120% (Supplementary Fig. 13), with approximately 57% decrease in the on current compared with that of the flat state for the blue phototransistor.

Despite their stable operation under stretching, their optical performance was inferior to that of the phototransistors based on inorganic materials. We ascribe this inferior performance primarily to the poor gate dielectric performance in our device, rather than the isQDSN itself, because the phototransistors fabricated using the isQDSN with a rigid gate dielectric layer (SiO_2 , 300 nm), non-stretchable source and drain electrodes (Cr/Au, 7/70 nm), and highly doped silicon substrate as a bottom gate electrode, exhibited substantially improved performance. For example, a photoresponsivity of ~ 80 mA W^{-1} and photodetectivity of $\sim 8.0 \times 10^8$ Jones were obtained for the green phototransistor with an illumination of green light (Supplementary Fig. 14). Supplementary Table 4 shows a detailed comparison of the electrical and optoelectronic

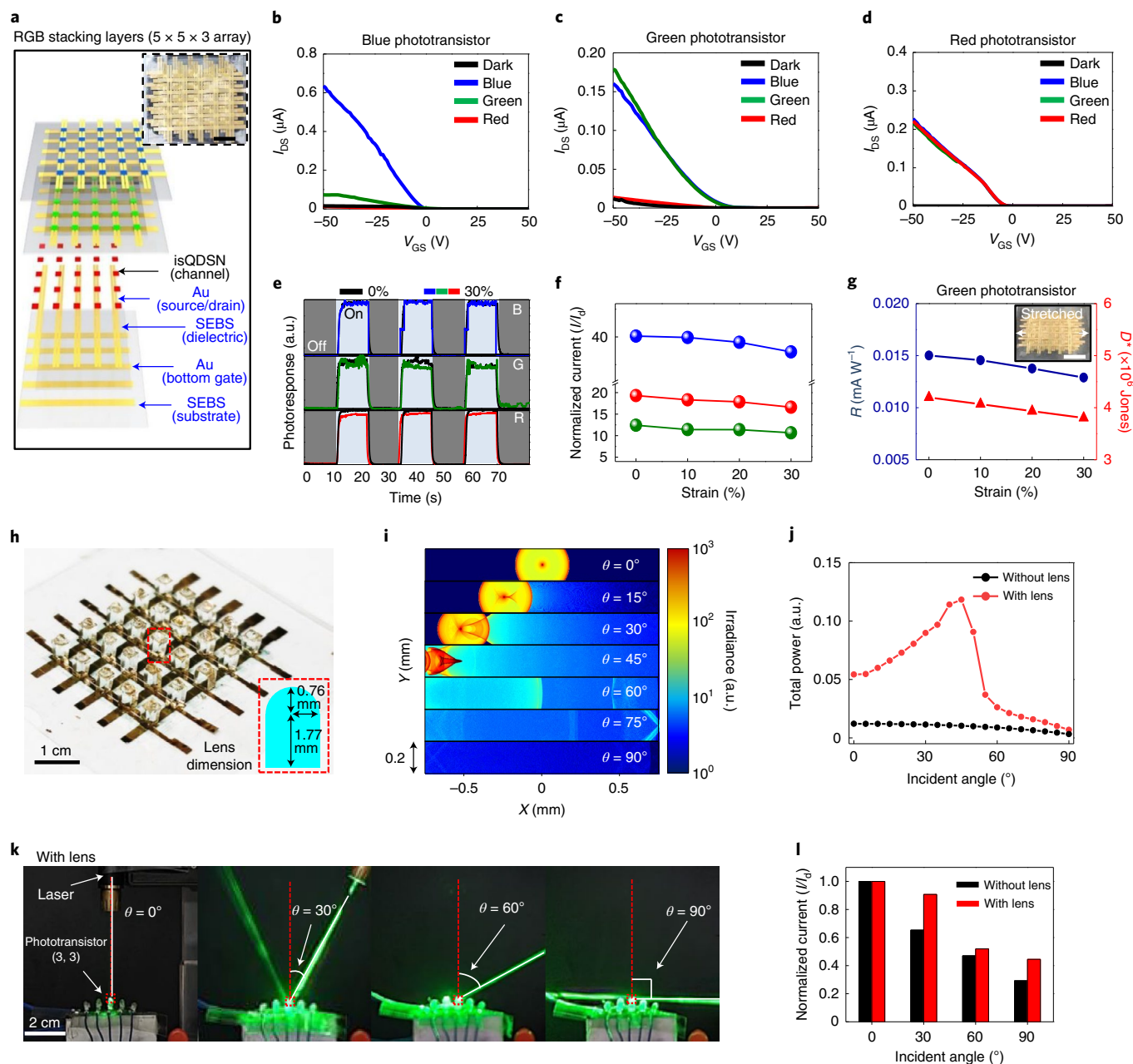


Fig. 3 | Characterization of the intrinsically stretchable phototransistor. **a**, Schematic of the intrinsically stretchable phototransistor array. R, G and B arrays are stacked in a misaligned manner. The inset shows a photograph of the intrinsically stretchable phototransistor array. Scale bar, 10 mm. **b–d**, Photoresponses of the blue phototransistor (**b**), green phototransistor (**c**) and red phototransistor (**d**) under light illumination of 450, 525 and 630 nm wavelength, respectively ($L_{\text{ch}} = 150 \mu\text{m}$; $W_{\text{ch}} = 1.5 \text{ mm}$). **e**, Normalized photocurrents of the red, green and blue phototransistors under periodic on/off illumination conditions before stretching (black curve) and after 30% stretching (blue, green and red curves). **f**, Normalized photocurrents of phototransistors with respect to increasing strains from 10% to 30%. **g**, Photoresponsivity (left) and photodetectivity (right) of stretchable phototransistors under different strains up to 30%. Scale bar, 10 mm. **h**, Photograph of the phototransistor array integrated with the deformable lens array. The inset shows the design parameters of a single lens. **i**, Simulation results of the light-focusing effect by the lens for light irradiation from various angles. **j**, Simulation result comparing the power delivered by the incident light from various angles, with and without lens integration. **k**, Photographs of the experimental setup for measuring photocurrents after lens array integration with lights irradiated at various incident angles. **l**, Comparison of normalized photocurrents for phototransistors with and without lens array integration at various incident angles.

performances and parameters of the phototransistors in rigid and stretchable formats. The optoelectronic performance could be further improved by scaling down the device dimensions (L_{ch} values of 2, 5, 10, 15 and 20 μm on a rigid substrate and 10 μm for intrinsically stretchable format), and these devices also exhibited high uniformity (Extended Data Figs. 5 and 6). It should also be noted that

other types of QD (such as CdS and PbS) can be used to increase the photodetection range including ultraviolet and infrared ranges (Extended Data Figs. 7 and 8).

The intrinsically stretchable phototransistor array can be potentially applied to wearable electronics. For wearable device applications, the mechanical stability of the material and device is highly

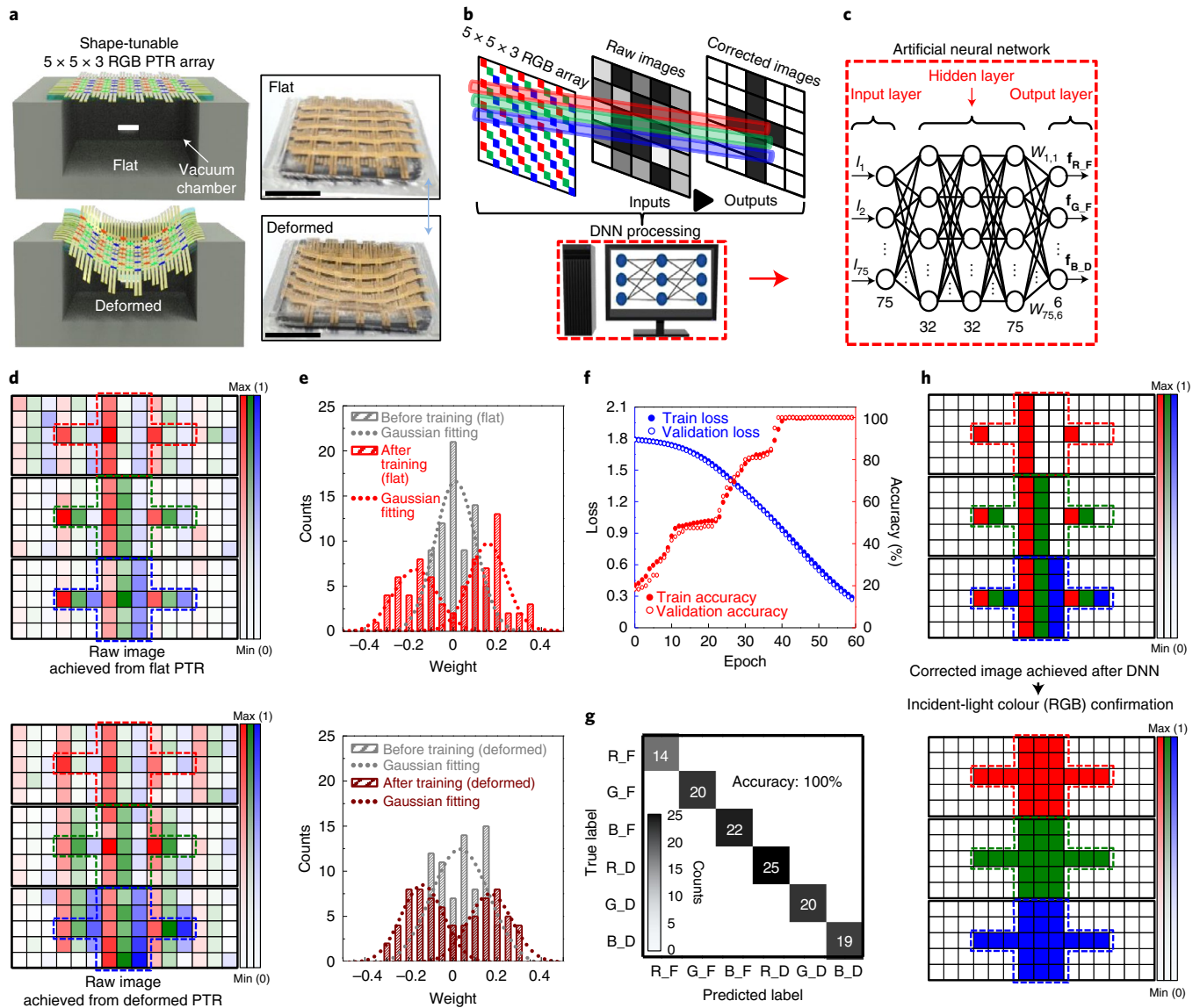


Fig. 4 | High-density imaging demonstration using the intrinsically stretchable phototransistor array on a curved surface with deep learning algorithms. **a**, Schematic and photographic images of $5 \times 5 \times 3$ phototransistor array in flat (top) and deformed states (bottom). Scale bars, 10 mm. **b**, Schematic showing the image sensing with a deep learning algorithm. **c**, Diagram of the developed artificial neural network. **d**, Normalized current signals of the R, G and B image patterns in flat (top) and deformed (bottom) states. **e**, Histograms and Gaussian fitting curves of weights connected to the $f_{R,F}$ (top) and $f_{B,D}$ (bottom) patterns with respect to the number of training epochs. **f**, Loss and accuracy values of training and validation with respect to the training epoch. **g**, Confusion matrix of the classification results. **h**, Corrected image patterns achieved after the application of DNN (top) from flat and deformed images, and confirmation of the incident-light colour through the colour-sensing algorithm (bottom).

desirable. After passivating the array with an SEBS encapsulation layer, a PBS solution was dropped on the $5 \times 5 \times 3$ array to observe any changes in the electrical performance (Supplementary Fig. 15a). The encapsulated device under the PBS solution exhibited stable photocurrents and dark currents over 3 h (Supplementary Fig. 15b). The array was conformally laminated on human skin (Supplementary Fig. 15c). The device exhibited stable photocurrents even after bending deformation (Supplementary Fig. 15d (image), Supplementary Fig. 15e (photoresponse) and Supplementary Fig. 16 (measurement setup)).

Integration of lens for wide field-of-view demonstration

To maximize the benefit of our intrinsically stretchable phototransistor array, we integrated a lens system for the demonstration of a wide field of view. The detailed fabrication and integration

processes of the polydimethylsiloxane (PDMS) lens array can be found in Methods, Fig. 3h and Extended Data Fig. 9a. The effect of the lens array for the wide field-of-view photodetection was first verified by a simulation, showing that the incident light is concentrated on the active layer due to light refraction by the lens surface and light guiding by the internal reflection of the lens post. At an incident angle of 0° , only the focusing effect is seen. At an incident angle of 30° , both focusing and guiding effects are clearly observed. At incident angles of 60° or larger, only the guiding effect is detected (Fig. 3i). Thus, compared with the case without lens integration, the incident light can be more effectively focused and delivered to the phototransistor array, with the maximum efficiency at the incident angle of 45° where both light-focusing effect and guiding effect occur simultaneously (Fig. 3j). Supplementary Note 5 provides further details of the lens simulation.

For the actual comparison of the photocurrents of the intrinsically stretchable phototransistors with and without the integration of the PDMS lens array, the 5×5 array was mounted on a hemispherical surface with a radius of curvature of approximately 20 mm. Using a laser, light was irradiated on the middle pixel (3, 3) at incident angles of 0° , 30° , 60° and 90° , and the photocurrents were measured using the green phototransistor for both cases (Fig. 3k and Extended Data Fig. 9b). The measured photocurrents were normalized with the dark currents, and the magnitudes of the normalized photocurrents for the different incident angles were compared (Fig. 3l). As a result, the phototransistor with the integrated PDMS lens array exhibited substantially enhanced photocurrent generation at all incident angles. Compared with the photocurrent when light was irradiated at 0° , the bare phototransistor exhibited 70.8% decrease in the photocurrent when light was irradiated at 90° , whereas the phototransistor with the PDMS lens array exhibited only 55.5% decrease in the photocurrent when light was irradiated at 90° .

Imaging demonstration with a deep learning algorithm

The intrinsically stretchable $5 \times 5 \times 3$ phototransistor array can be conformally laminated onto a curvilinear surface (Supplementary Fig. 17). A high areal coverage of the device can be achieved owing to its intrinsic stretchability, which does not require special interconnect designs for shape tunability. To verify the shape-tunable optoelectronic performance of the intrinsically stretchable phototransistor array, a custom-built deformation stage based on a vacuum-controlled chamber was prepared (Fig. 4a; top and bottom show the flat and deformed state; left and right show the schematic and corresponding photograph, respectively). The phototransistor array could be deformed into hemispherical shapes (maximum strain is 10.4% at a radius of curvature of 18.4 mm) by controlling the internal pressure of the vacuum chamber stage (Supplementary Figs. 18 and 19 and Supplementary Note 6). Within the maximum-strain range, the stacked phototransistor layers acted as if they were a unibody device without any physical delamination of the layers, as confirmed by the simulation results and photocurrent measurements at the applied strain of 10% (Extended Data Fig. 10). Incident-coloured light patterns were detected under the flat and deformed states of the $5 \times 5 \times 3$ phototransistor array. The colour of the incident light could be verified by checking how many phototransistors in a single pixel (R, G and B) of the phototransistor array have responded to the light (Supplementary Fig. 20).

We also applied a DNN (Fig. 4b) that offers two advantages: (1) compensation of optical aberrations and noise during mechanical deformations and (2) enhancement of photodetection accuracy. A neural network model consisting of 75 input neurons, six output neurons and three hidden layers (layer sizes of 32, 32 and 75, respectively) was devised, where an activation function of the rectified linear unit was used on all the nodes of the hidden layers, and a softmax function was used on the output nodes (Fig. 4c and Supplementary Fig. 21). Supplementary Fig. 22 and Supplementary Note 7 provide further details of the DNN algorithm.

Before beginning with the DNN algorithm, the input photocurrent data of the $5 \times 5 \times 3$ phototransistor array were measured using peripheral component interconnect extensions for instrumentation system with a LabVIEW-based custom-made program (NI LabVIEW 2020) (Supplementary Figs. 23 and 24 and Supplementary Note 8). Supplementary Figs. 25 and 26 show a schematic and images of the operation and setup, respectively. A classification task was implemented using the DNN algorithm on a raw photocurrent dataset containing 600 samples for six pattern images (Fig. 4d; R, G, and B array data for the flat (top) and deformed (bottom) states). In this experiment, the initial weight was randomly selected according to the Gaussian distribution, and gradually potentiated or depressed according to the number of epochs (Fig. 4e; top and bottom show the flat- and deformed-state data under the incident

red-coloured light). During training, the ratio of training, validation and testing samples was 360, 120 and 120 samples, respectively (Supplementary Figs. 27–31). The loss (difference between the given and learned data) and accuracy (probability of obtaining the correct answer) values were derived by changing the learning rate and number of batch sizes/epochs. The training was performed by applying a learning rate of 0.001, batch size of 200 and epoch of 60. As a result, at 60 epochs, the training accuracy and loss were 100% and 0.288, respectively, and the validation accuracy and loss were 100% and 0.270, respectively (Fig. 4f).

Figure 4g shows the confusion matrix of the classified results. Six image patterns (each label was assigned as R_F, G_F, B_F, R_D, G_D and B_D, where F and D refer to the flat and deformed states, respectively) were successfully classified with a high accuracy of 100%. The 25 paired images (Supplementary Fig. 32, left) randomly chosen by the test data corresponded to the expected outcomes (Supplementary Fig. 32, right). The output data after applying the DNN algorithm are shown in Fig. 4h (top), where three corrected images are shown corresponding to the original pattern of the mask. By considering the light adsorption properties of R, G and B QDs, we can verify the types of light colours that were irradiated to the phototransistor array. Evidently, each incident-light colour was successfully validated using the proposed colour-sensing algorithm (Fig. 4h, bottom, and Supplementary Fig. 20). These results demonstrate that sensing RGB light colour with the DNN can compensate for optical aberrations and noises that occur during mechanical deformations and enhance the accuracy of photodetection^{40,41}.

Conclusion

We presented a shape-tunable multiplexed phototransistor array using an intrinsically stretchable and colour-sensitive semiconducting nanocomposite. The composition of the isQDSN was analysed via XPS, transmission electron microscopy and atomic force microscopy, and the optoelectronic and mechanical performances of the isQDSN-based phototransistors were characterized. The isQDSN features high colour sensitivity, efficient charge transport and mechanical stretchability. A $5 \times 5 \times 3$ multiplexed RGB phototransistor array was fabricated using the isQDSN films without sacrificing areal density, and a DNN algorithm was applied to compensate for optical aberrations and/or noises, resulting in the enhancement of image-sensing accuracy even under various mechanical deformations. The optoelectronic performance of the phototransistors could be improved further owing to the application of high-resolution patterning to the active device area. In addition, the integration of PDMS lenses on the fabricated phototransistor array could enlarge the field of view. The shape-tunable phototransistor array with the DNN algorithm made it possible to realize the precise imaging of the projected RGB light patterns under both flat and curved states. The technologies for the facile shape-tuning capability (intrinsic stretchability), multispectral sensing capability without colour filters, deformable lens integration for a wide field of view, and compensation of optical aberration and noise using the DNN algorithm can be highly beneficial to next-generation artificial vision applications, such as electronic/prosthetic eyes, miniaturized wide field-of-view cameras and mobile electronics/robotics.

Online content

Any methods, additional references, Nature Research reporting summaries, source data, extended data, supplementary information, acknowledgements, peer review information; details of author contributions and competing interests; and statements of data and code availability are available at <https://doi.org/10.1038/s41565-022-01160-x>.

Received: 21 September 2021; Accepted: 23 May 2022;

Published online: 07 July 2022

References

- Jung, I. et al. Dynamically tunable hemispherical electronic eye camera system with adjustable zoom capability. *Proc. Natl Acad. Sci. USA* **108**, 1788–1793 (2011).
- Li, Z., Wang, Y. & Xiao, J. Mechanics of curvilinear electronics and optoelectronics. *Curr. Opin. Solid State Mater. Sci.* **19**, 171–189 (2015).
- Li, Z. & Xiao, J. Strain tunable optics of elastomeric microlens array. *Extreme Mech. Lett.* **4**, 118–123 (2015).
- Lee, H. et al. Stretchable organic optoelectronic devices: design of materials, structures, and applications. *Mater. Sci. Eng. R Rep.* **146**, 100631 (2021).
- Yokota, T. et al. A conformable imager for biometric authentication and vital sign measurement. *Nat. Electron.* **3**, 113–121 (2020).
- Lee, W. et al. Two-dimensional materials in functional three-dimensional architectures with applications in photodetection and imaging. *Nat. Commun.* **9**, 1417 (2018).
- Gu, L. et al. A biomimetic eye with a hemispherical perovskite nanowire array retina. *Nature* **581**, 278–282 (2020).
- Ko, H. C. et al. A hemispherical electronic eye camera based on compressible silicon optoelectronics. *Nature* **454**, 748–753 (2008).
- Song, Y. et al. Digital cameras with designs inspired by the arthropod eye. *Nature* **497**, 95–99 (2013).
- Kim, M. S. et al. An aquatic-vision-inspired camera based on a monocentric lens and a silicon nanorod photodiode array. *Nat. Electron.* **3**, 546–553 (2020).
- Choi, C. et al. Curved neuromorphic image sensor array using a MoS₂-organic heterostructure inspired by the human visual recognition system. *Nat. Commun.* **11**, 5934 (2020).
- Choi, C. et al. Human eye-inspired soft optoelectronic device using high-density MoS₂-graphene curved image sensor array. *Nat. Commun.* **8**, 1664 (2017).
- Zhang, K. et al. Origami silicon optoelectronics for hemispherical electronic eye systems. *Nat. Commun.* **8**, 1782 (2017).
- Rao, Z. et al. Curvy, shape-adaptive imagers based on printed optoelectronic pixels with a kirigami design. *Nat. Electron.* **4**, 513–521 (2021).
- Cho, K.-S. et al. Color-selective photodetection from intermediate colloidal quantum dots buried in amorphous-oxide semiconductors. *Nat. Commun.* **8**, 840 (2017).
- Kim, J. et al. A skin-like two-dimensionally pixelized full-color quantum dot photodetector. *Sci. Adv.* **5**, eaax8801 (2019).
- Ding, Y. et al. Stacking-mode confined growth of 2H-MoTe₂/MoS₂ bilayer heterostructures for UV–vis–IR photodetectors. *Nano Energy* **49**, 200–208 (2018).
- Matsuhisa, N. et al. Printable elastic conductors by in situ formation of silver nanoparticles from silver flakes. *Nat. Mater.* **16**, 834–840 (2017).
- Choi, S. et al. Highly conductive, stretchable and biocompatible Ag–Au core–sheath nanowire composite for wearable and implantable bioelectronics. *Nat. Nanotechnol.* **13**, 1048–1056 (2018).
- Son, D. et al. An integrated self-healable electronic skin system fabricated via dynamic reconstruction of a nanostructured conducting network. *Nat. Nanotechnol.* **13**, 1057–1065 (2018).
- Xu, J. et al. Highly stretchable polymer semiconductor films through the nanoconfinement effect. *Science* **355**, 59–64 (2017).
- Sim, K. et al. Fully rubbery integrated electronics from high effective mobility intrinsically stretchable semiconductors. *Sci. Adv.* **5**, eaav5749 (2019).
- Wang, W. et al. Strain-insensitive intrinsically stretchable transistors and circuits. *Nat. Electron.* **4**, 143–150 (2021).
- Jung, D. et al. Highly conductive and elastic nanomembrane for skin electronics. *Science* **373**, 1022–1026 (2021).
- Wang, S. et al. Skin electronics from scalable fabrication of an intrinsically stretchable transistor array. *Nature* **555**, 83–88 (2018).
- Guan, Y.-S. et al. Air/water interfacial assembled rubbery semiconducting nanofilm for fully rubbery integrated electronics. *Sci. Adv.* **6**, eabb3656 (2020).
- Lee, W. S. et al. Designing high-performance CdSe nanocrystal thin-film transistors based on solution process of simultaneous ligand exchange, trap passivation, and doping. *Chem. Mater.* **31**, 9389–9399 (2019).
- Kagan, C. R. et al. Colloidal quantum dots as platforms for quantum information science. *Chem. Rev.* **121**, 3186–3233 (2020).
- Zhao, Q. et al. Enhanced carrier transport in strongly coupled, epitaxially fused CdSe nanocrystal solids. *Nano Lett.* **21**, 3318–3324 (2021).
- Shin, M. et al. Polythiophene nanofibril bundles surface-embedded in elastomer: a route to a highly stretchable active channel layer. *Adv. Mater.* **27**, 1255–1261 (2015).
- Sim, K., Rao, Z., Ershad, F. & Yu, C. Rubbery electronics fully made of stretchable elastomeric electronic materials. *Adv. Mater.* **32**, 1902417 (2020).
- Xu, J. et al. Multi-scale ordering in highly stretchable polymer semiconducting films. *Nat. Mater.* **18**, 594–601 (2019).
- Seo, H. et al. Durable and fatigue-resistant soft peripheral neuroprosthetics for in vivo bidirectional signaling. *Adv. Mater.* **33**, 2007346 (2021).
- Zhou, F. et al. Optoelectronic resistive random access memory for neuromorphic vision sensors. *Nat. Nanotechnol.* **14**, 776–782 (2019).
- Choi, M. et al. Wearable red–green–blue quantum dot light-emitting diode array using high-resolution intaglio transfer printing. *Nat. Commun.* **6**, 7149 (2015).
- Li, M. et al. Light-induced interfacial phenomena in atomically thin 2D van der Waals material hybrids and heterojunctions. *ACS Energy Lett.* **4**, 2323–2335 (2019).
- Milleville, C. C. et al. Directional charge transfer mediated by mid-gap states: a transient absorption spectroscopy study of CdSe quantum dot/ β -Pb_{0.33}V₂O₅ heterostructures. *J. Phys. Chem. C* **120**, 5221–5232 (2016).
- Luo, L.-B. et al. A highly sensitive perovskite/organic semiconductor heterojunction phototransistor and its device optimization utilizing the selective electron trapping effect. *Adv. Opt. Mater.* **7**, 1900272 (2019).
- Oh, J. Y. et al. Stretchable self-healable semiconducting polymer film for active-matrix strain-sensing array. *Sci. Adv.* **5**, eaav3097 (2019).
- Li, Z. & Xiao, J. Mechanics and optics of stretchable elastomeric microlens array for artificial compound eye camera. *J. Appl. Phys.* **117**, 014904 (2015).
- Lee, G. J., Choi, C., Kim, D.-H. & Song, Y. M. Bioinspired artificial eyes: optic components, digital cameras, and visual prostheses. *Adv. Funct. Mater.* **28**, 1705202 (2018).

Publisher's note Springer Nature remains neutral with regard to jurisdictional claims in published maps and institutional affiliations.

© The Author(s), under exclusive licence to Springer Nature Limited 2022

Methods

Synthesis procedure of isQDSN. For the synthesis of the isQDSN composite, cadmium oxide (CdO, >99.99%), selenium (Se, 99.99%), zinc acetate (Zn(OAc)₂, 99.99%), elemental sulfur powder (S, 99.0%), 1-octadecene (technical grade, 90%), oleic acid (technical grade, 90%), trioctylphosphine (90%), tributylphosphine (95%), ethyl alcohol (99.5%, anhydrous), chlorobenzene (99.8%, anhydrous) and chloroform (99%, anhydrous) were purchased from Aldrich Chemical. Styrene-ethylene-butylene-styrene (H1221) was purchased from Asahi Kasei. DPP-DTT (PDPP2T-TT-OD) was purchased from Ossila.

Green CdSe/ZnS QDs with alloyed interfaces were synthesized by reacting metal oleate complexes with trioctylphosphine selenide and trioctylphosphine sulfide at high temperatures. Blue and red QDs were synthesized by controlling the core sizes of the CdSe/ZnS QDs using similar methods. Detailed synthesis methods for red, green and blue QDs have been reported earlier³⁷. Furthermore, 0.1 g QDs, PDPP2T-TT-OD and SEBS were dissolved in 30 ml chlorobenzene and stirred for 1 d.

Fabrication and characterization of phototransistor arrays. Intrinsically stretchable phototransistor arrays were fabricated using all the stretchable components. An SEBS elastomer of 80 mg ml⁻¹ in toluene (H1062, Asahi Kasei) was used as a stretchable handling substrate (0.2 mm in thickness) and 180 mg ml⁻¹ in toluene for encapsulation (0.2 mm in thickness). Gate electrodes were patterned on the SEBS substrate using a shadow mask with thermally evaporated gold (50 nm in thickness). For the dielectric layer, an SEBS elastomer of 60 mg ml⁻¹ in toluene (H1052, Asahi Kasei) was spin coated onto an octadecyl trimethoxysilane (OTS)-treated SiO₂/Si wafer (1,000 rpm/1 min). The OTS treatment of the SiO₂/Si wafer was conducted according to a previous report³⁷. The dielectric layer was then transferred onto the SEBS handling substrate with gate electrode patterns. For the semiconducting channel layer, the as-prepared isQDSN solution containing red CdSe/ZnS QDs was spin coated onto an OTS-treated SiO₂/Si wafer (1,000 rpm/1 min). The channel layer was then transferred onto the dielectric layer of the SEBS handling substrate. The encapsulation layer, SEBS elastomer of 180 mg ml⁻¹ in toluene (H1062, Asahi Kasei), was spin coated onto an OTS-treated SiO₂/Si wafer (500 rpm/1 min). The source and drain were thermally evaporated (50-nm-thick Au) onto the encapsulation SEBS layer using a shadow mask. Finally, the encapsulation SEBS layer was transferred onto the SEBS substrate. For green and blue phototransistor arrays, the devices were fabricated using the same method, except using the isQDSN solution containing different types of QD for the semiconducting channel.

The photocurrent measurements of the individual arrays were performed using a parameter analyser (B1500A, Agilent) equipped with a probe station (MSTECH). Red/green/blue light-emitting diodes were used as the light sources. A manual one-dimensional stretcher was used to apply the strain after the device was mounted onto the stage.

Fabrication and integration of the deformable lens array. The lens array was fabricated by first preparing a mould using a three-dimensional printer, followed

by pouring and curing 30:1 PDMS. The mould was designed to yield a lens array with a single lens radius of 0.76 mm and a post height of 1.77 mm, to cover the entire active pixel area of the intrinsically stretchable phototransistors in the 5 × 5 array configuration. After detaching the PDMS lens array from the mould, the lens array was integrated on the phototransistor array.

Data availability

Source data are provided with this paper. All data that support the findings of this study are included in the main text and Supplementary Information. Any additional materials and data are available from the corresponding authors on reasonable request.

Code availability

The source codes are available from the corresponding authors upon reasonable request.

Acknowledgements

We acknowledge the following funding sources: Institute for Basic Science (IBS-R006-D1, IBS-R006-A1, and IBS-R015-D1) (J.-K.S., J.K., J.Y., J.H.K., H.J., K.K., S.-H.S., S.Y., H.C., J.J., W.B., S.L., M.L., H.J.K., M.S., T.H., D.-H.K. and D.S.); the National Research Foundation of Korea (NRF) grant funded by the Korea government (MSIT) (no. 2020R1C1C1005567) (D.S.); and the Basic Science Research Program through the NRF funded by the Ministry of Education (2021R111A1A01060389) (J.H.K.).

Author contributions

J.-K.S., J.K., J.Y., J.H.K., T.H., D.-H.K. and D.S. designed the experiments, analysed the data and wrote the paper. J.-K.S., J.K., J.Y. and J.H.K. fabricated the phototransistor array and performed the characterization of individual devices and multiplexed arrays. J.Y. and K.K. developed the deep learning algorithm. H.J. performed the theoretical analysis of the mechanics. All the authors discussed the results and commented on the manuscript.

Competing interests

The authors declare no competing interests.

Additional information

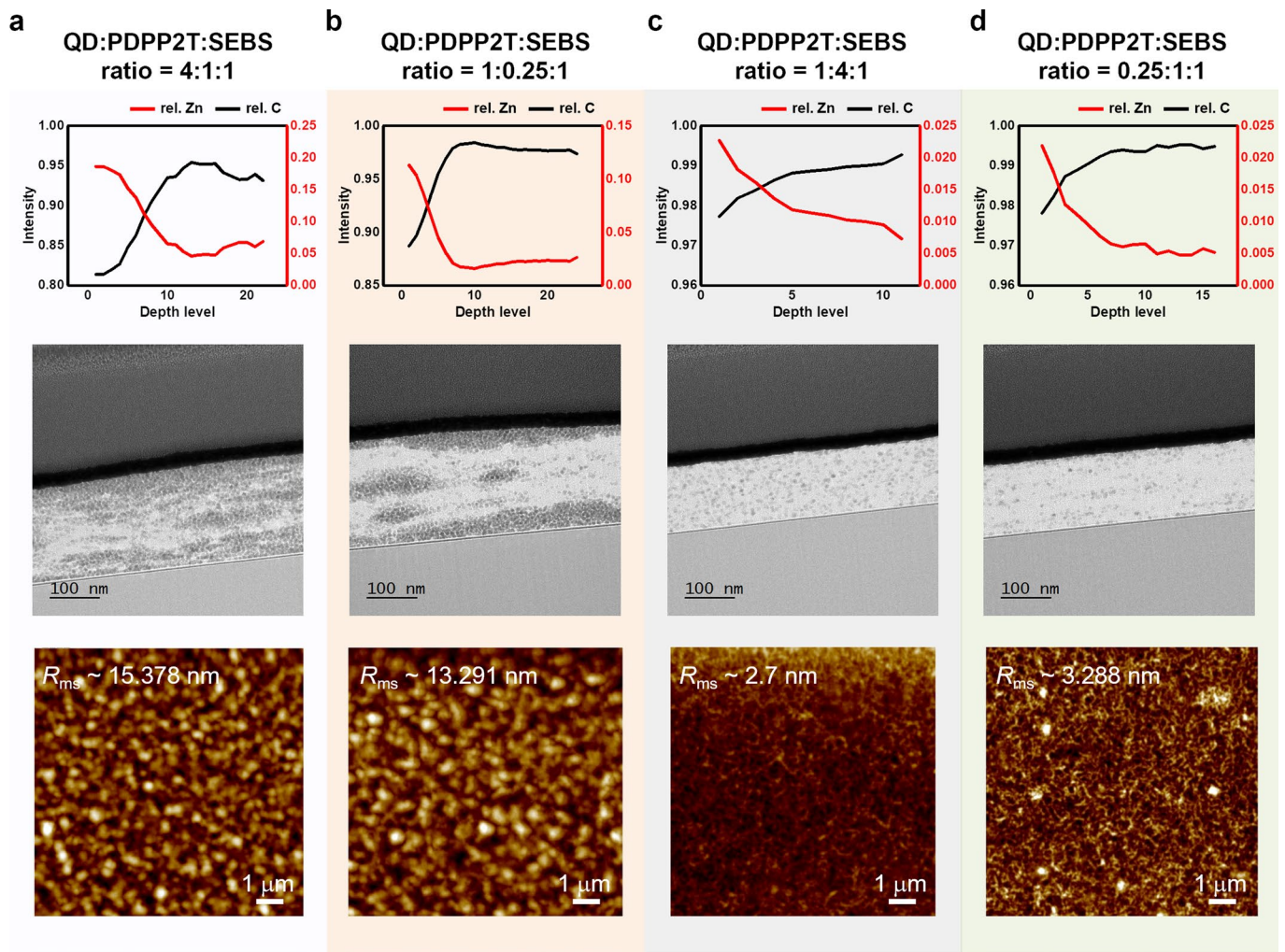
Extended data is available for this paper at <https://doi.org/10.1038/s41565-022-01160-x>.

Supplementary information The online version contains supplementary material available at <https://doi.org/10.1038/s41565-022-01160-x>.

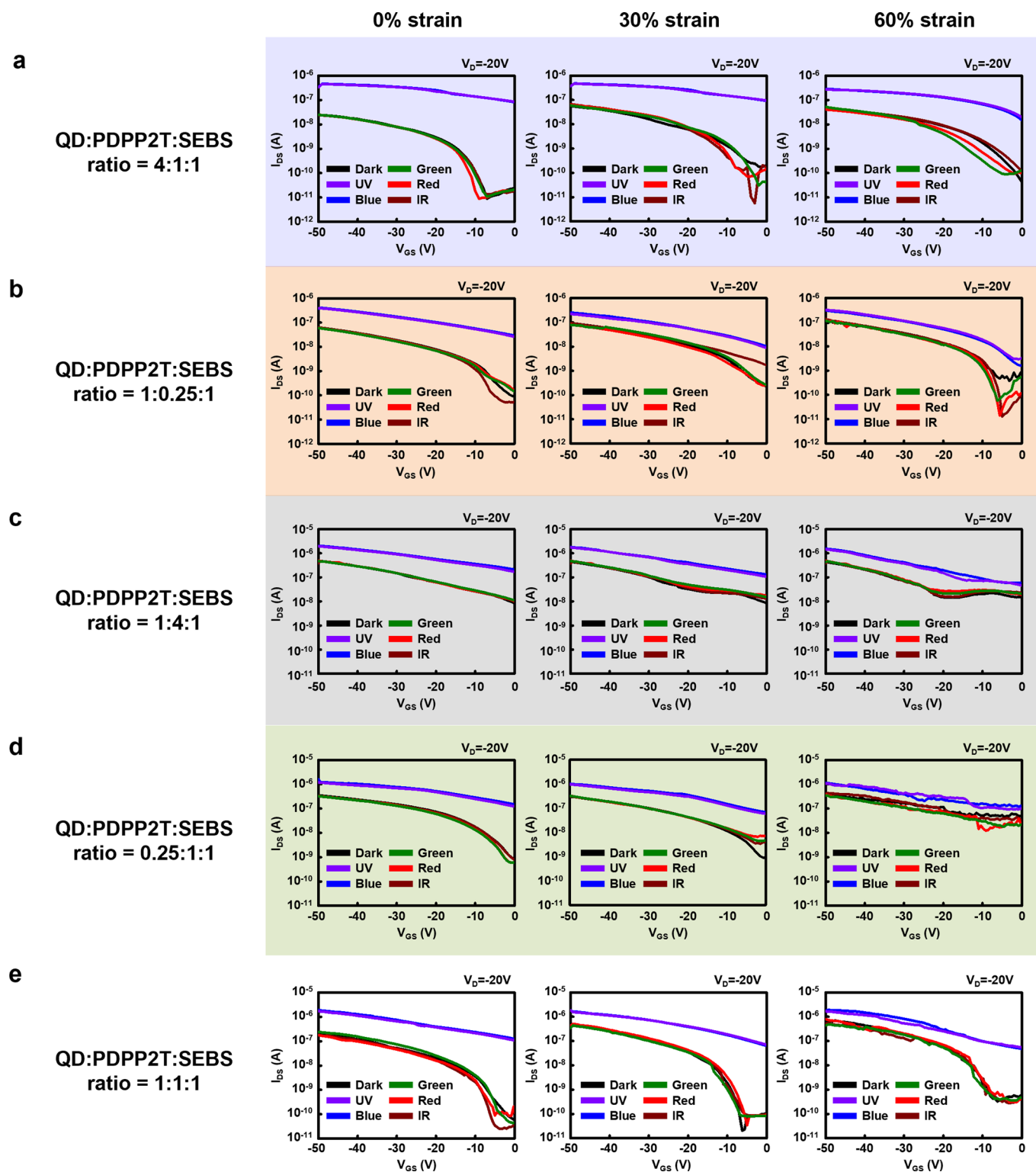
Correspondence and requests for materials should be addressed to Taeghwan Hyeon, Dae-Hyeong Kim or Donghee Son.

Peer review information *Nature Nanotechnology* thanks the anonymous reviewers for their contribution to the peer review of this work.

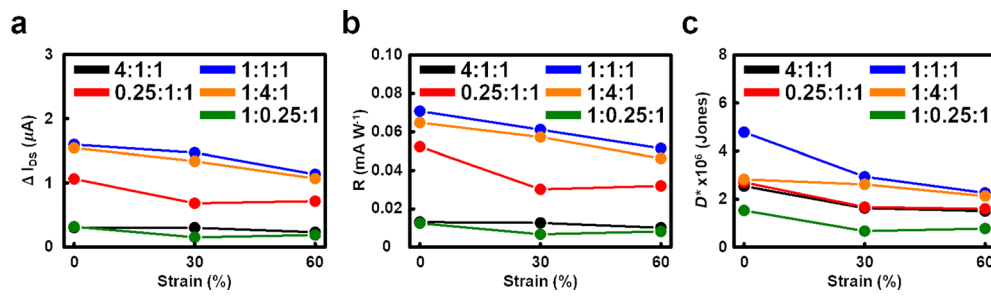
Reprints and permissions information is available at www.nature.com/reprints.



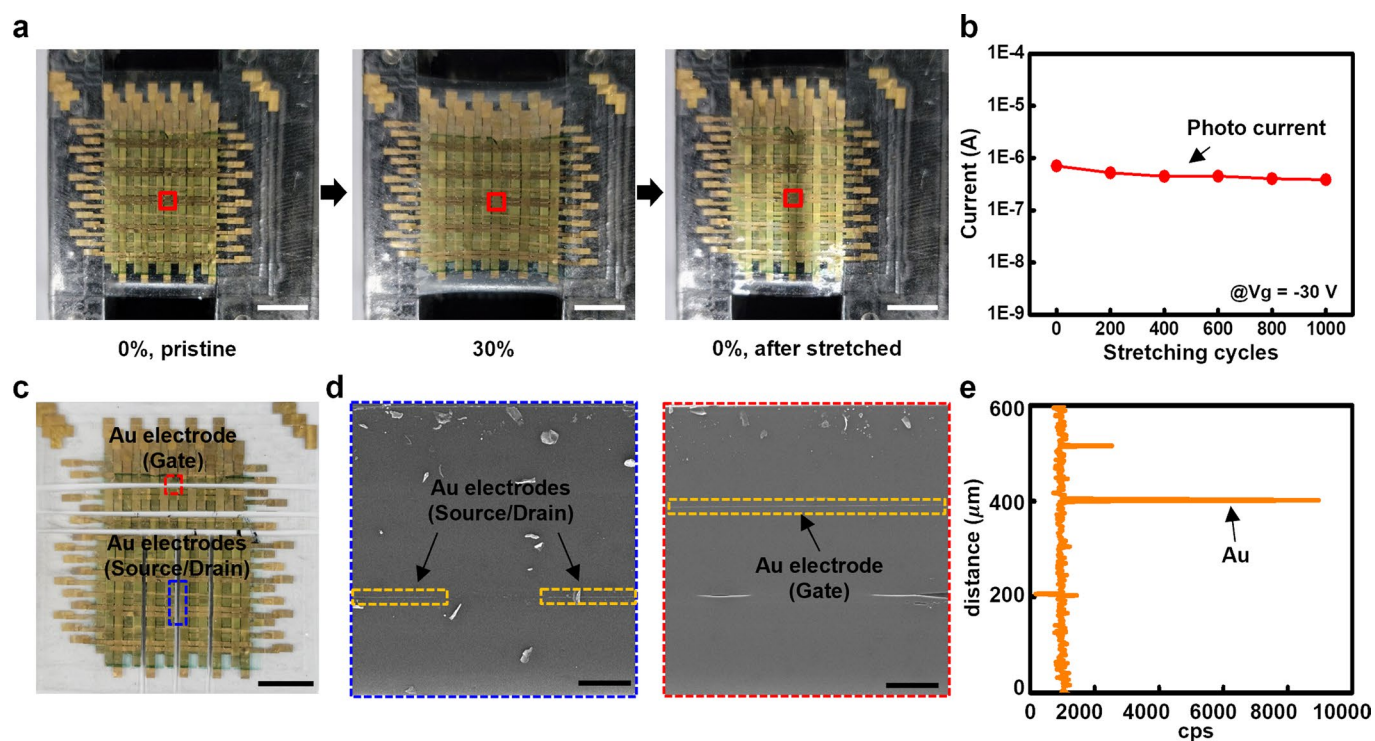
Extended Data Fig. 1 | Depth-XPS analyses, high-resolution cross-sectional TEM analyses, and AFM analyses of isQDSNs with various QD:PDPP2T:SEBS ratios. Depth-XPS analyses, high-resolution cross-sectional TEM analyses, and AFM analyses of isQDSNs with various QD:PDPP2T:SEBS ratios. The ratios are a, 4:1:1, b, 1:0.25:1, c, 1:4:1, and d, 0.25:1:1.



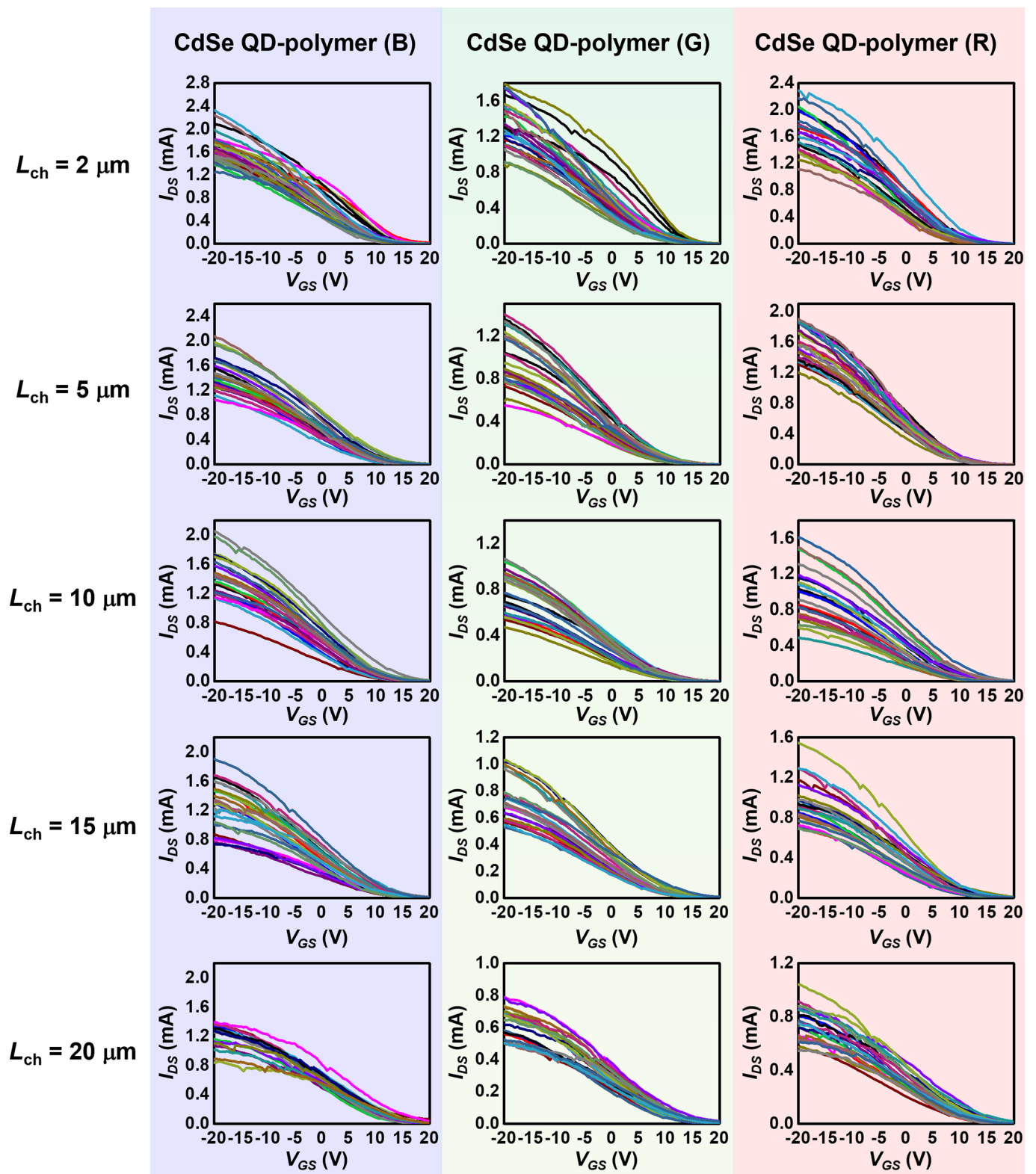
Extended Data Fig. 2 | Transfer characteristics of phototransistors employing isQDSNs with various QD:PDPP2T:SEBS ratios, under various applied strains. Transfer characteristics of phototransistors employing isQDSNs with various QD:PDPP2T:SEBS ratios, under various applied strains. The QD:PDPP2T:SEBS ratios are a, 4:1:1, b, 1:0.25:1, c, 1:4:1, d, 0.25:1:1, and e, 1:1:1. The dimensions of the phototransistors are $L_{ch} = 150 \mu\text{m}$ and $W_{ch} = 1.5 \text{ mm}$.



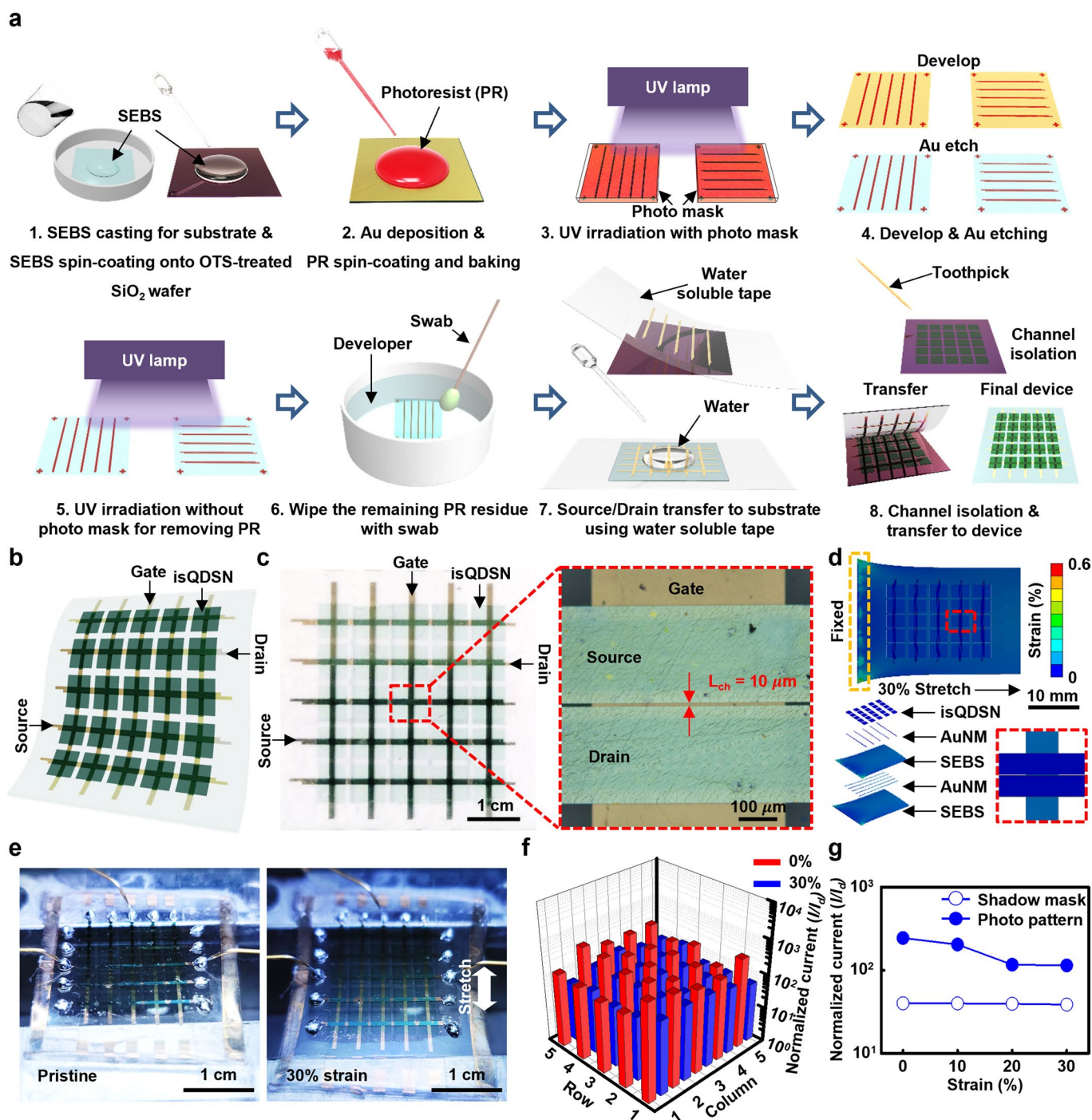
Extended Data Fig. 3 | Strain and composition dependent change of device characteristics. Strain and composition dependent change of device characteristics. Changes in the a, on-photocurrent, b, photoresponsivity, and c, photodetectivity of the phototransistors employing isQDSNs with various QD:PDPP2T:SEBS ratios, under various applied strains ($L_{\text{ch}} = 150 \mu\text{m}$, $W_{\text{ch}} = 1.5 \text{ mm}$).



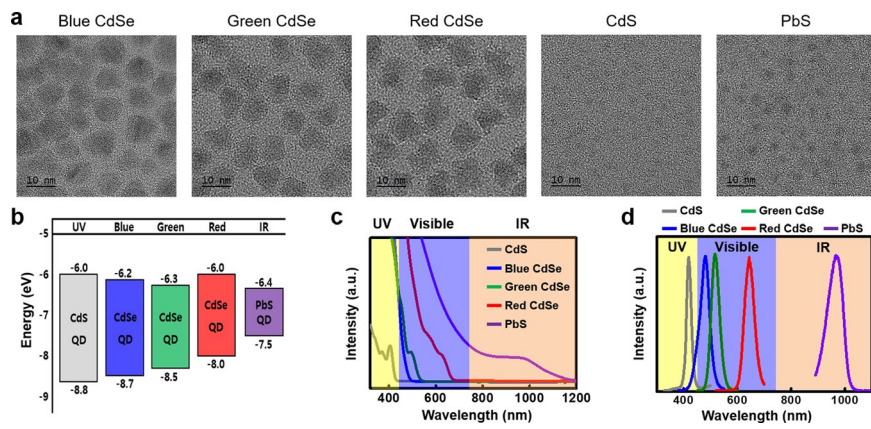
Extended Data Fig. 4 | 1,000 cyclic stretching test results at 30% strain. 1,000 cyclic stretching test results at 30% strain. **a**, Photographs of the $5 \times 5 \times 3$ phototransistor array during the stretching test. Scale bar, 10 mm. **b**, Photocurrents of the phototransistor taken after every 200 stretching cycles with 30% strain, until 1,000 cycles. **c**, Photograph of the $5 \times 5 \times 3$ phototransistor array after stretching test, denoting the regions for cross-sectional SEM analyses. Scale bar, 10 mm. **d**, Cross-sectional SEM images of the $5 \times 5 \times 3$ phototransistor array, taken from the regions of red- and blue-dotted boxes in **c**. Scale bar, $100 \mu\text{m}$ (red dot: horizontal axis, blue dot: vertical axis). **e**, Line scan EDS result of the gold electrode in red-dotted box region.



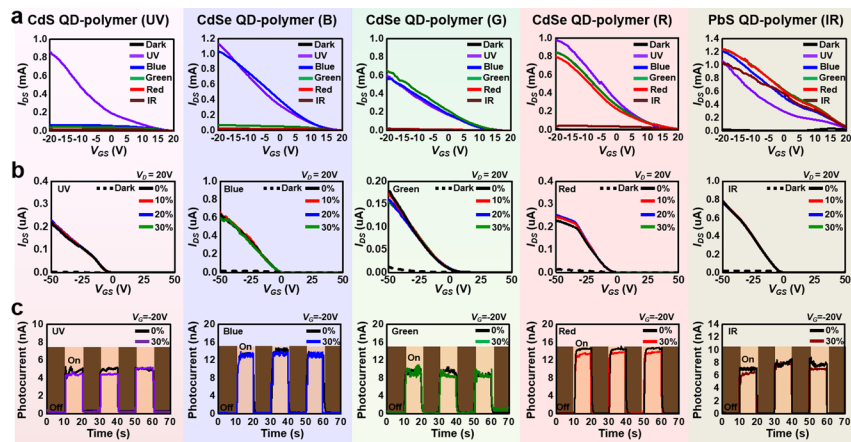
Extended Data Fig. 5 | Transfer characteristics of phototransistors fabricated on rigid SiO_2 substrates with scaled-down channel lengths ($L_{\text{ch}} = 2, 5, 10, 15,$ and $20 \mu\text{m}$, $W_{\text{ch}} = 1.5 \text{ mm}$), demonstrating high device-to-device uniformity and enhanced photocurrent generations. Transfer characteristics of phototransistors fabricated on rigid SiO_2 substrates with scaled-down channel lengths ($L_{\text{ch}} = 2, 5, 10, 15,$ and $20 \mu\text{m}$, $W_{\text{ch}} = 1.5 \text{ mm}$), demonstrating high device-to-device uniformity and enhanced photocurrent generations.



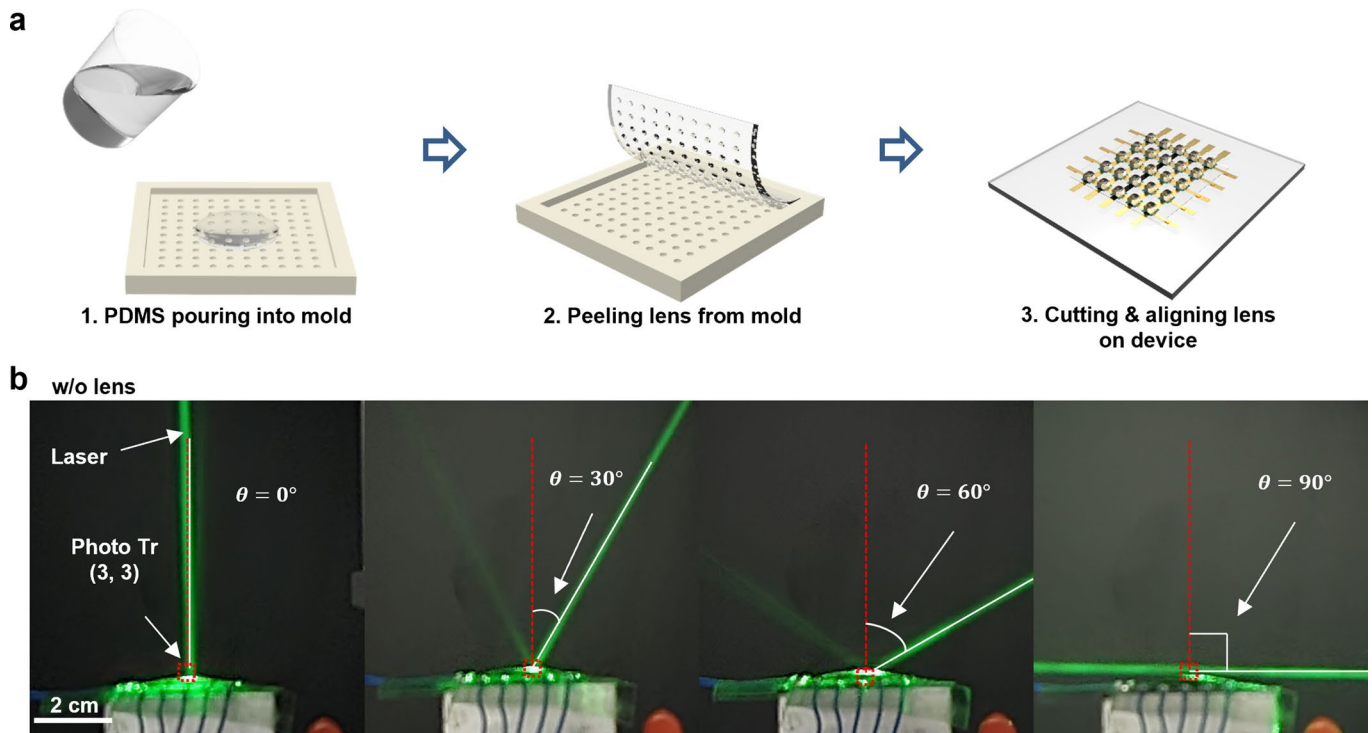
Extended Data Fig. 6 | Intrinsically stretchable phototransistor array with reduced channel lengths. Intrinsically stretchable phototransistor array with reduced channel lengths. **a**, Schematic illustration of device fabrication using photolithography. **b**, Schematic illustration of the 5×5 phototransistor array. **c**, Photographic image of a 5×5 phototransistor array (left) and magnified image of a single phototransistor in the red-dotted box (right) ($L_{\text{ch}} = 10 \mu\text{m}$, $W_{\text{ch}} = 1.5 \text{ mm}$). **d**, Simulation results showing the strain induced in the phototransistors at the applied strain of 30%. **e**, Photographic images taken during the photocurrent measurements at flat (left) and stretched (right) states. **f**, Cumulative data of normalized photocurrents measured during flat and stretched modes. **g**, Comparison between photocurrents of the phototransistors fabricated using shadow masking and photolithography.



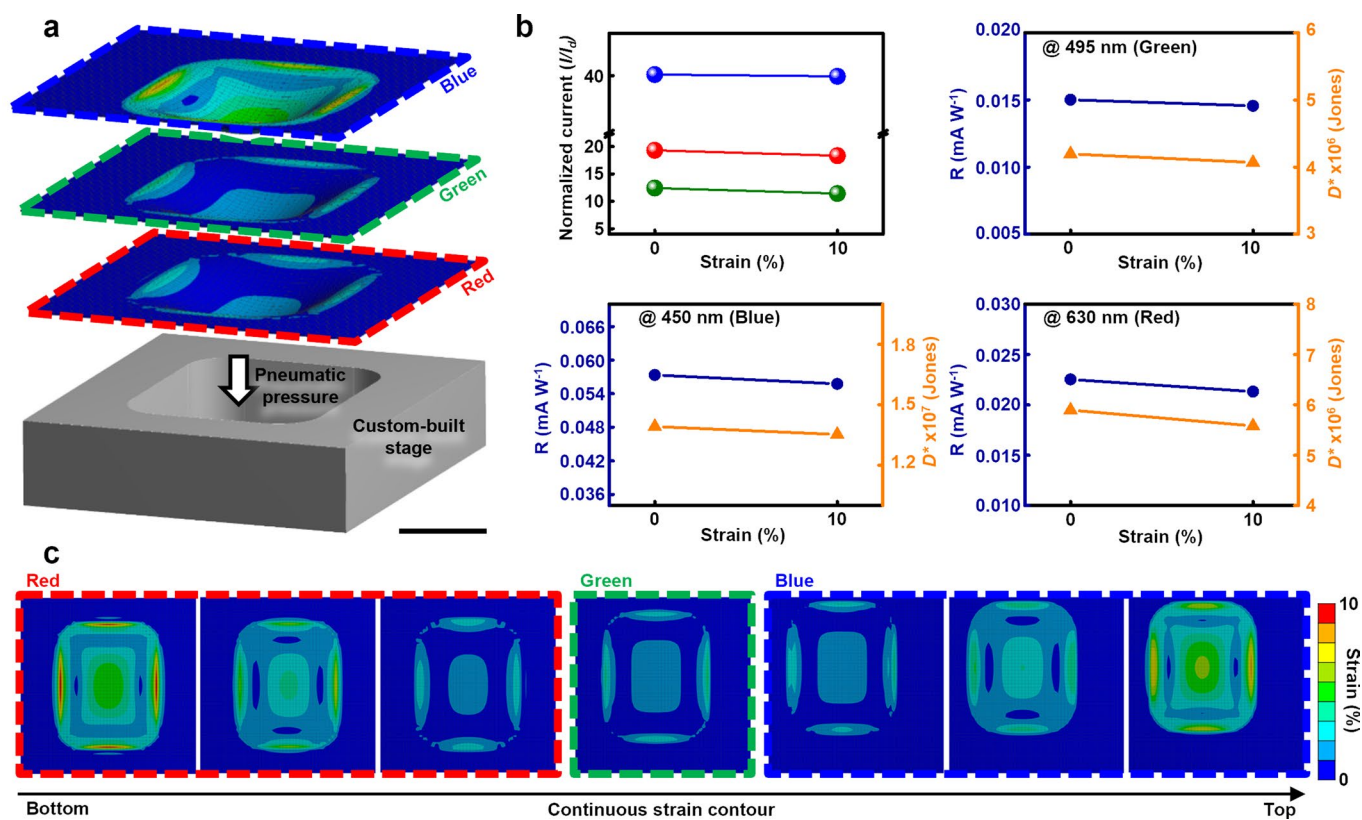
Extended Data Fig. 7 | Different types of size-tunable QDs and their absorption properties. Different types of size-tunable QDs and their absorption properties. **a**, TEM images of different QDs used to develop isQDSNs for tunable colour selectivity. **b**, Energy band diagram of different QDs. **c**, **d**, Absorption spectra of different QDs.



Extended Data Fig. 8 | Phototransistors based on 5 different types of iQDSNs for wide-spectrum photodetection. Phototransistors based on 5 different types of iQDSNs for wide-spectrum photodetection. **a**, Photoresponses of the phototransistors using the different iQDSNs, fabricated on rigid SiO_2 substrates ($L_{\text{ch}}=150\ \mu\text{m}$, $W_{\text{ch}}=1.5\ \text{mm}$). **b**, Photoresponses of the stretchable phototransistors using different iQDSNs under various strains ($L_{\text{ch}}=150\ \mu\text{m}$, $W_{\text{ch}}=1.5\ \text{mm}$). **c**, Light responses of the stretchable phototransistors using different iQDSNs.



Extended Data Fig. 9 | Schematic illustrations of the PDMS lens array fabrication and photographs of the experimental setup for measuring photocurrents with lights irradiated at various incident angles, without integration of the lens array. a, Schematic illustrations of the PDMS lens array fabrication and **b**, Photographs of the experimental setup for measuring photocurrents with lights irradiated at various incident angles, without integration of the lens array.



Extended Data Fig. 10 | FEA results of the phototransistor array during mechanical deformation, normalized photocurrents, photoresponsivities, and photodetectivities of phototransistors, and the continuous strain contour in R, G, B layers during mechanical deformation. a, FEA result of the $5 \times 5 \times 3$ phototransistor array showing the strain exerted in each R, G, B layer as an exploded view, during mechanical deformation by mounting on the custom-built stage and applying strain. **b**, Normalized photocurrents, photoresponsivities, and photodetectivities of R, G, B phototransistors before and after applying 10% strain. **c**, The continuous strain contour in R, G, B layers during mechanical deformation by mounting on the custom-built stage and applying strain.